Order Parameters and Algorithmic Approaches for Detection and Demarcation of Interfaces in Hydrate−Fluid and Ice−Fluid Systems

Bjørn Steen Sæthre,*,[†] Alex C. Hoffmann,[†] and David van der Spoel[‡]

[†]Institute of Physics & Technology, University of Bergen, 5007 Bergen, Norway

[‡]Uppsala Centre for Computational Chemistry, Science for Life Laboratory, Department of Cell & Molecular Biology, University of Uppsala, SE-75124 Uppsala, Sweden

ⓈSupporting Information

ABSTRACT: Some aspects of the use of order parameter fields in molecular dynamics simulations to delimit solid phases containing water, namely ice and hydrate, in both hydrophilic and hydrophobic fluids are examined; this includes the influences of rectangular meshes and of filtering on the quality of these parameters. Three order parameters are studied: the mass density, ρ; an angular tetrahedrality measure, S_g (Chau and Hardwick, *Mol. Phys.* **1998**, *93*, 511); and the water−dimer dihedral angle, F_4 (Rodger et al. *Fluid Phase Equilib.* **1996**, *116*, 326). The parameters are studied to find their ability to distinguish between bulk phases, their consistency in different environments, their noise susceptibility, and their ability to demarcate the interface region. Spatial sampling and filtering are covered in detail, and some temporal features are illustrated by using autocorrelation maps. The parameters are employed to determine the position of interfaces as functions of time and, with the capillary wave fluctuation method (Hoyt et al. *Phys. Rev. Lett.* **2001**, *86*, 5530; *Math. Comput. Simul.* **2010**, *80*, 1382), to estimate solid−fluid interfacial stiffnesses, with partial success for the hydrophilic/hydrophobic-type interfaces.
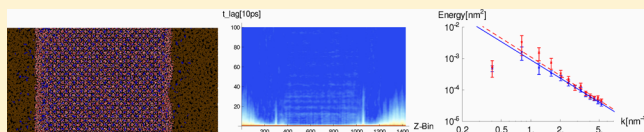
1. INTRODUCTION

The oil and gas industries are aiming at more complex extraction scenarios offshore: in deeper and colder waters with longer subsea production lines carrying complex multiphase flows and at the same time attempting to fully automate the extraction process. One consequence is that understanding hydrate flow assurance[1] and plug mitigation[2−4] becomes ever more important.

This requires an understanding of hydrate nucleation,[5,6] (anti-)agglomeration and adhesion,[7−17] growth kinetics,[18−22] and flow properties.[23−25] All these hydrate properties are related fundamentally to understanding the physico-chemical properties of the hydrate−fluid, hydrate−mineral, and hydrate−metal interfaces.[3,26] Due to the large variability of production environments and the unpredictability[27] of experimental studies of solid interfaces mainly due to surface adsorption of impurities, idealized computer simulations of the hydrate interfaces are becoming an attractive choice to increase our understanding of the dynamics[28] and even obtain quantitative interfacial thermodynamic data.

Good spatial order parameters are essential in the molecular modeling of the dynamics of phase transitions and of interfacial phenomena both generally[29] and for aqueous phases specifically.[30−33] High-precision order parameters are the foundation for the best methods to infer the solid/fluid interfacial free energy, namely the capillary wave fluctuation (CWF) method[34] and the metadynamics[35] method for accelerated thermodynamic integration.

Some important characteristics determine the effectiveness and utility of an order parameter field:

- distinguishability — How good is the parameter for separating the relevant phases?
- demarcation ability — How good is the parameter for locating and describing the interfacial region?
- noise susceptibility — How well does the parameter tolerate noise while maintaining precision?
- consistency — Does the parameter give values similar to those of identical bulk phases in different system geometries and in differing chemical environments?
- sampling properties — Does the parameter tolerate different spatiotemporal sampling schemes, and what are the optimal sampling rates?

In this work, three order parameters are tested for use in molecular dynamics with solid phases of water in both aqueous and organic fluid environments with the above considerations in mind, focusing particularly on the quality of interfacial demarcation for use in the CWF method.

First brief descriptions of the models, the phases, and the geometrical configuration in the interfacial systems are given. Subsequently the order parameters used and their regions of applicability are defined, and some approaches to interface demarcation for each one are discussed. Then the order parameters and their dynamic behavior are examined, dealing with the hydrophilic/hydrophobic interfaces hydrate-II−oil and ice-IH−oil. Thereafter two hydrophilic/hydrophilic interfaces, hydrate-II−water and ice-IH−water, are treated in a similar manner. These sections focus on the influence of the spatial and

temporal sampling rates and filtering on the qualitative consistency of the order parameter field. The consistency of each order parameter is evaluated on the basis of a small set of variability criteria. Finally, the article concludes with a brief discussion of the main results. As an application of the order parameters, an attempt is made to find the stiffnesses of selected hydrophilic/hydrophobic interfaces by the CWF method.

2. METHODOLOGY

2.1. Geometric System Configurations. Two different geometries have been proposed for the analysis of surface properties, namely a pseudo-one-dimensional (1D) strip[34,36] and a full two-dimensional (2D)[37,38] geometry. Both types of systems involve a planar slab solid phase, which will be denoted by A in this paper, and a fluid phase, denoted by B, in an elongated simulation box.

For the pseudo-1D configurations the system dimensions that have been used in the past were roughly 80×4×82 face-centered cubic (FCC) unit cells (UCs) in an atomic system[36] and 30×4×60 UCs for a succinonitrile molecular crystal-melt system.[39] In the succinonitrile system this corresponded to absolute dimensions of 19.2 × 2.5 × 38.8 nm. For the 2D configurations, a setup of 20×20×45 UCs of simple FCC metallic crystals has been used.[37] These workers and others[36] have kept the dimension normal to the solid slab roughly double the size of the largest interface dimension. This was done to prevent interface−interface correlation across the periodic boundaries[40] and interference of interface and bulk-crystal phonons.

The advantages of using a full 2D interface are the greater number of accessible fluctuation modes available and a reduction of edge effects.[37] A drawback for stiff interfaces is the relatively smaller magnitude of capillary waves present in this geometry compared to the pseudo-1D case of similar size.[41] The pseudo-1D configuration is predicted to have a linear scaling of the fluctuations with size and therefore likely a better signal-to-noise ratio than a 2D interface whose fluctuations scale-up logarithmically.[42] A disadvantage of the 1D approach, however, is that more simulations are needed to resolve, e.g., the interfacial free energy out of stiffness measurements.[34,43] This is because crystals with less symmetry have more degrees of freedom for the accessible vibrational modes.

In the end, a pseudo-1D geometry was chosen for all the molecular systems studied in this work for the following reasons:

To capture the higher amplitude, long-wavelength CWFs well, a certain minimum linear in-plane dimension is needed.[44,45] If the system dimension is too small, these natural frequencies of the system are inaccessible. Also, if the normal-to-interface dimension of the system is too small relatively speaking, there will be problems resolving the capillary waves with the fixed amplitude resolution and, as mentioned, an increased risk of interface cross-correlations. Lastly it is desirable to maximize the physical simulation time and minimize the computational effort (i.e., total atom number).

Consistent with the papers cited above, the following guidelines were used here in setting up the geometries:

1. The B-A-B rectangular slab topology with periodic boundary conditions was adopted to obtain a system with sensible surface/volume ratio.
2. A roughly 50/50 volume ratio of solid/fluid was used in the initial system. The volume of solvent needed depends strongly on the size (inhomogeneity scale) of solvent molecules.
3. A pseudo-1D strip geometry was adopted, as mentioned, where one in-interface dimension, L, was significantly larger than the other, b, such that $L/b \geq 7$ (this was 20 in ref 36).
4. To reduce the possibility of correlated interface fluctuations, the normal dimension Z is kept 2−3 times the size of the length scale associated with the interface; i.e., $Z \approx 2L$.

2.1.1. Hydrate Systems. For the pseudo-1D systems of hydrate-II−oil, in view of previous work and the considerations above, a 9×2×9 UC structure II solid slab was used, immersed in fluid such that the hydrate volume fraction became about 0.5. This had starting dimensions of about 15.5 × 3.44 × 28.5 nm. The increased width is an adaptation to

improve the spatial distribution of the long-chained octane molecules and to reduce their tendency for artificial alignment, forced by the geometry, in the interface region. For the similar hydrate-II−water systems, a 10×1×10 UC structure II hydrate slab was used, immersed in water to give a hydrate volume fraction at 0.5. The dimensions of this system are approximately 17.5 × 1.75 × 35.0 nm after equilibration (Figure 1a,b).
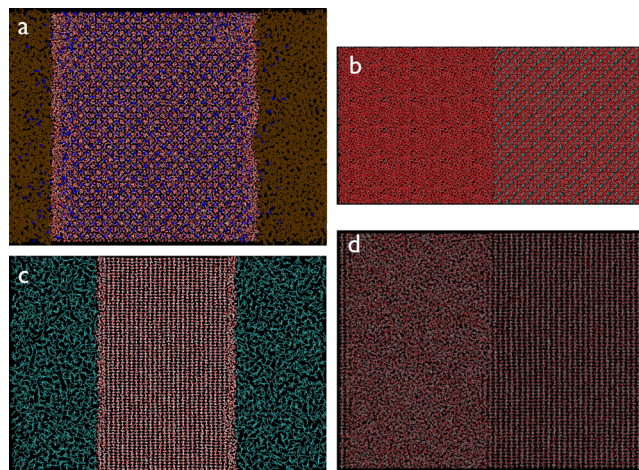
Figure 1. Configurations of interface systems: (a) hyd(100)−oil, (b) hyd(100)−water, (c) ice(0001)−oil, and (d) ice(0001)−water. The B-A-B topology creates two interfacial regions. We denote the interface B-A as number 1 and the interface A-B as number 2.

2.1.2. Ice Systems. The ice-IH−fluid systems were prepared from rectangular slabs[46] and then replicated up to the larger crystals studied. Using the criteria outlined above, the starting configuration was a 36×3×15 UC (0001) ice crystal, with a starting dimension of 16.2 × 2.34 × 11.0 nm. Thereafter this crystal was brought in contact with the fluid, water or oil, extending the normal dimension to approximately 23−25 nm.

2.1.3. Fluid Models and Force Fields. The four-site TIP4P−ice water model was used in this in this work,[47] together with the OPLS$_{UA}$ force field[48] for the propanes filling the large cavities and for the oil phase (1-octane).

2.1.4. Simulation Details. The classical leap-frog integrator was used to integrate Newton's equations. Neighbor search was handled by Verlet lists, updated every 10 steps in simulations and every 5 steps in equilibrations, with a cutoff of 0.85 nm for the hydrate−water simulations and a cutoff of 0.9 nm for all the other simulations. The time step was 2 fs in all cases. The SETTLE algorithm[49] was used to constrain the water molecules.

For electrostatics, the PME algorithm[50] was employed with cubic or quintic interpolation and Fourier space grid size of 0.12−0.15 nm. Cubic interpolation was used with the smaller grid in the hydrophobic/hydrophilic systems, and quintic interpolation was used with the larger grid to improve parallel performance in the hydrophilic systems.

A Berendsen[51] thermostat and barostat were utilized in the equilibration stage. The isothermal compressibility of hydrate was initially estimated to be 1.2×10^{-5} bar^{-1}. The compressibility of the liquid phases was set to 4×10^{-5} bar^{-1} (water) or 8×10^{-5} bar^{-1} (oil). All box vectors were scaled independently, but no shear was introduced.

A stochastic velocity rescaling scheme[52] was employed to impose the canonical ensemble on the simulations runs. All simulations were performed with the GROMACS package.[53]

2.2. Order Parameters. The order parameters used in this work are of two different types: the density is based on a static meshing of space, whereas the tetrahedral[54] and F_4[55] parameters are defined on a per-molecule basis. This puts an inherent limit of the resolution obtainable using the density field, whereas the F_4 parameters' resolution is originally limited only by the floating-point numerical precision. In practical use, however, the per-molecule parameters must be projected onto a spatial

mesh as well. This is done by a rectangular 3D binning scheme, and results in the F_4 and tetrahedrality parameters are also resolution-limited by the mesh widths.

The basic aim of the interface demarcation algorithm is to reduce the 3D order parameter field to a mathematical 2D surface for each time step in the simulation trajectory. Some schemes to achieve this is listed at the end of this section, following the definition of the order parameter fields.

2.2.1. Density. For phases in which there is a clear difference in bulk density, like the solid-water−hydrocarbon interfaces, mass density is an obvious order parameter.

In this work the mass density is obtained by meshing the simulation box at a selection of time steps with a Cartesian 3D grid and by counting the number of particles within each mesh point, giving the local density in each mesh point. Consistent with the rectangular slab geometries in this work, a rectangular mesh is used where the resolution is significantly higher in the dimension normal to the interface:

$$\rho_i = N_i / V_{cell} = N_i / A\Delta z, \quad \Delta z \ll L \tag{1}$$

2.2.2. A Local Tetrahedral Order Parameter for Solid−Fluid Interfaces of Water. An order parameter that is particularly well suited to the water molecule was proposed by Chau and Hardwick.[54] The parameter gauges the degree to which nearest-neighbor molecules are tetrahedrally coordinated. The parameter is defined in two parts, in terms of an angle and a distance. The distance part is

$$S_k = \sum_{k=1}^{4} \left(\frac{(\vec{r}_k - \mathbf{r})^2}{4\mathbf{r}^2} \right) \tag{2}$$

where $\mathbf{r}$ is the arithmetic mean of the $\vec{r}_k$'s, which are the distances between the oxygen atom of the molecule under consideration and the oxygens in the nearest-neighbor water molecules. For a perfect tetrahedral arrangement, $S_k = 0$.

The angular part is given by

$$S_g = \frac{3}{32} \sum_{i=1}^{3} \sum_{j=i+1}^{4} \left(\hat{\vec{r}}_i \cdot \hat{\vec{r}}_j + \frac{1}{3} \right)^2 \tag{3}$$

where $\hat{\vec{r}}_i$, $\hat{\vec{r}}_j$ are unit vectors pointing from the oxygen atom in the molecule under consideration to the oxygen atoms of the ith and jth nearest-neighbor molecules. Note that $\cos(\theta_{tetrahedron}) = -1/3$, and hence $S_g = 0$, when all angles are perfect tetrahedral angles. This definition is different than that used by others,[31] to make it easier to compare to the distance part S_k.

Only the angular part S_g will be used in this work, due to its greater absolute difference in values between solid and fluid phases.

2.2.3. The Water Dimer Dihedral Angle Parameter, F_4. Another suitable order parameter to distinguish water, ice, and hydrate is the parameter F_4,[55] defined for each water molecule as

$$F_4 = \langle \cos(3\Phi_{dihedral}) \rangle \tag{4}$$

where $\Phi_{dihedral}$ is the dihedral angle between two water dimers and where the spatial average is over all the dimers that are part of the molecule. The dihedral angle is chosen as that between the furthest separated H−O−H⋯O−H dihedral in the water dimer.

This order parameter is well suited not only for hydrate−water systems but also to distinguish clearly between ice-IH and hydrate in that it is especially sensitive to planar ring structures, which are prevalent in hydrate but not in ice-IH.

2.2.4. Order Parameter Fields and Interface Demarcation Schemes. The present implementation of a full four-dimensional (4D) order parameter field, being based on a fixed, rectangular mesh, has the following freely selectable variables:

1. species of particle over which the field is computed (for density field only)
2. tangential (to interface) mesh binwidth
3. normal (to interface) mesh binwidth
4. filter order (or width, always expressed in number of bins) of spatial Gaussian filter in the normal direction
5. temporal sampling rate and averaging

It is useful to look at various subsets of the above factors in isolation, in the following.

The Gaussian filter has the form

$$K^o[k] = \frac{1}{N} \left\{ \exp\left[-\frac{k^2}{2\sigma^2} \right] \right\}_{k=\{-n,n\}} \tag{5}$$

where $\sigma = n/2$ and the normalization $N = \sum_{k=-n}^{n} \exp[(-k^2/2\sigma^2)]$, and all indices are given modulo N in this equation and eq 7 below. The Gaussian filter order, which may also be referred to as the width of the Gaussian filter, is defined as $o = \text{abs}[n]$.

The filtering is achieved by using the kernel in a periodic convolution (to exploit the periodic nature along the Z axis):

$$F[n] = K^o[n] * \phi[n] \equiv \sum_{p=0}^{N-1} K[p] f[(n-p) \bmod N] \tag{6}$$

where $\phi[n]$ is the order parameter filtered and $K[i]$ is shifted to be defined between $i = 0$ and $i = N - 1 = 2n$.

The following diagnostics will be used to discuss which set of values for these parameters provides the optimal spatiotemporal resolution, distinguishability, and consistency of the interface, for the purpose of studying the dynamics of the interfacial region.

> **smoothness criterion**: the sum-of-squares of the second central difference of the order parameter profiles in the direction of inhomogeneity in the systems,
>
> $$SS - (\nabla^2) = \sum_{p=0}^{N-1} (\nabla^2 \phi[p])^2$$
> $$= \sum_{p=0}^{N-1} (\phi[p+1] - 2\phi[p] + \phi[p-1])^2 \tag{7}$$
>
> **consistency criterion**: spatial−spatial cross-correlations within the same order parameter field, and between fields with different parameters
> **distinguishability**: distribution of order parameter values within each phase (possibly separated by species)
> **correct sampling**: temporal and spatial autocorrelation of the order parameter field

The method to separate bulk interface regions of the system from the three-dimensional (3D) order parameter fields, defined either via spatial meshing or on a per-molecule coordinate basis, will now be discussed. This method can be based on targeted searches, interpolation, edge detection schemes, or a combination of these approaches.

For an order parameter defined as a static 3D mesh on a planar slab geometry, a rectangular mesh must be used to maximize the resolution in the direction normal to the interface. The small volume of the resulting mesh elements, however, results in high-frequency noise in the order parameter fields. A low-pass filter is used to compensate for this effect, while taking care not to affect the interface positions or fluctuations significantly.

For an order parameter defined in a per-molecule sense, some filter is usually needed to make the mapping from location to order parameter value surjective (i.e., single-valued).

On the set of order parameters used here, at least one of the following algorithmic approaches can be used for demarcation of the interface.

> **Targeted search 1**: Find the nearest mesh point corresponding to a certain value of the order parameter, or if the mapping of order parameter to position is not unique in the interface region, average over all nearby points with the same order parameter.
> **Targeted search 2**: A small extension of variant 1 where the interface is demarcated by a small, predetermined interval of order parameter values. The interface position is set as the average position of molecules or mesh points having order parameters within this region.

Interpolation: Fit the order parameter profile to a certain functional and read out the interface position from fitted parameters.

Edge detection: Apply a difference filter to a profile, and thereafter locate the local maximum within the interface region.

The first approach together with pre-filtering of the profiles is possible, at least for the density field. The fourth approach was also attempted but suffered from the prevalence of edges/cliffs in both the filtered and unfiltered profiles. Not always, therefore, was the local maximum, even in the interface region, unique. The noise incurred from this was sufficient to make the interface location too ambiguous. A hard-coded implementation of the interpolation approach was not good enough to reliably locate the interface, since noise levels were appreciable in each raw profile.

In view of the above, results based only on targeted search 1 are presented here, but the intention is to investigate a combination of the second and third approaches in future work.

3. RESULTS

In interfaces of hydrophilic/hydrophobic character (Figures 1a,c), the phases are clearly distinguished by density. We therefore used the density order parameter defined in eq 1.

For the hydrophilic/hydrophilic test systems (Figures 1b,d), it is much more difficult to distinguishing the phases. For ice−water in particular, there is a small density difference and a very fuzzy, oscillatory density change at the interface, which makes it very difficult to demarcate the interface reliably with the density field, particularly in fine meshes. It is therefore necessary to employ the tetrahedral (eqs 2 and 3) and water dimer dihedral angle (F_4) parameters (eq 4).

Below we describe the four different systems one by one.

3.1. The Hydrate−Oil Interface. We first consider the pseudo-1D strip configuration $(100)[010]$ (the (100) Miller plane with a short interface bi-tangent in the $[010]$ coordinate direction) of saturated hydrate-II in octane (Figure 1a). Since we anticipate the need for using a relatively fine in-plane mesh and wish to optimize the counting statistics of the density field in each mesh point, a 1D strip geometry is imposed on the density field using a slightly non-square in-plane mesh.

3.1.1. Density Profiles. For each trajectory snapshot, results are available for all mesh points in the direction tangential to the interfaces. A sample density profile is shown in Figure 2a, obtained after filtering with a Gaussian filter. It can be seen that the densities of the hydrate-water framework and the octane phases are somewhat similar. Due to the inherent noise, the total density is not the best property to distinguish the phases, although it is feasible in this particular case. Instead the densities of the components can be studied separately, as shown for the same system in Figure 2c,d, making it possible to demarcate the interface region more clearly.

3.1.2. Effect of Filter Order. The filter width (order) is anticipated to have an important influence on resolution, phase distinguishability, interface demarcation, and smoothness (eq 7) of the profiles. The effects of normal binwidth and filter width are obviously interrelated, but they are considered separately here. As shown in Figures 5b and 3, the filter influences both the smoothness of the density profile, which follows a super-exponential increase with filter width, and the actual value of the bulk phase densities, as well as the width and position of the interfaces.

3.1.3. Effect of Binwidth. The effect of normal (bw) and tangential (bwn) binwidths on the profiles is shown in Figure 4a for water in the hydrate−oil systems. The interface positions are not very significantly affected by altering the tangential binwidth,
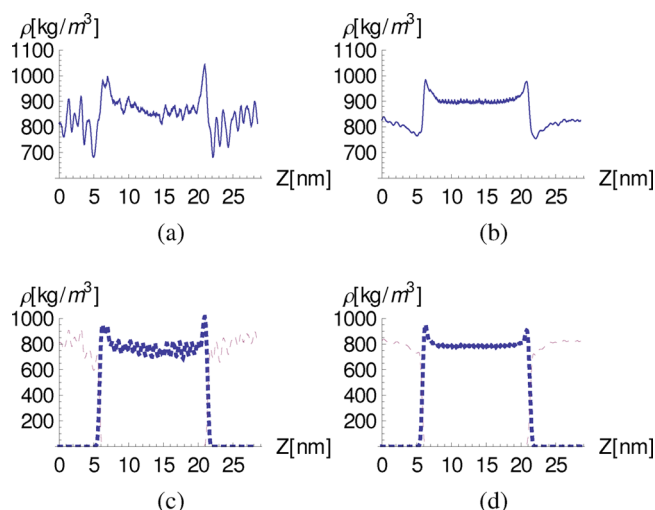

Figure 2. Density profiles for hydrate−oil, tangential binwidth (bw) = 0.6 nm, normal binwidth (bwn) = 0.02 nm, with smoothing by a Gaussian filter of order 20 at single trajectory snapshot: (a) from a single tangential mesh point, (b) average over all mesh points, (c,d) same as (a,b) with H_2O (thick blue dashed line) and 1-octane (thin red dotted line) studied separately.
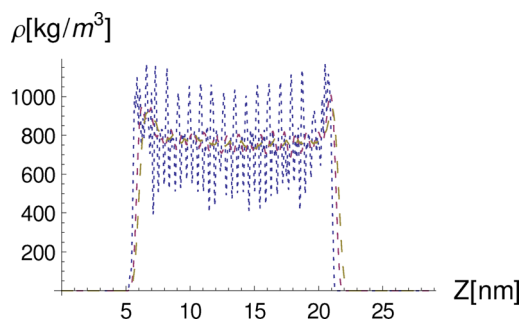

Figure 3. Effect of different Gaussian filter orders on the hydrate−oil density profiles based on water only: blue dotted line, order 5; red dash-dotted line, order 20; yellow dashed line, order 30 (for t = 100 ps, bw = 0.6 nm, bwn = 0.02 nm).

provided that the filter is applied. The absolute values of the densities are slightly affected, however, maybe due to an observed slight spatial correlation between bw and bwn. For the extremely small tangential binwidth of bnw = 0.15 nm (not shown in the figure, roughly equal to the radius of the water molecule), there are clear indications that the statistics of the density field are compromised, since, even with the filter, the profiles take on a distinctly non-smooth appearance. Keeping the normal bandwidth in the range bw = 0.3−0.6 nm, there is only little correlation (Figure 4b). Here it can also be seen that the normal binwidth does influence both the interfacial position and the width of the interface obtained. As the binwidth decreases the oscillations in density increase indicating progressively worsening counting statistics. The smoothness of a profile is plotted as a function of binwidth (bw) in Figure 5a showing an exponential decrease in noise with increased binwidth.

3.1.4. Cross Correlation between Density Profiles. The cross correlations between identically located density profiles using different filter orders is shown as a function of the in-interface position of the profile in Figure 6a. An enhancement of the correlation between the profiles with increasing filter order can be observed, indicating that the filtered profiles converge to a
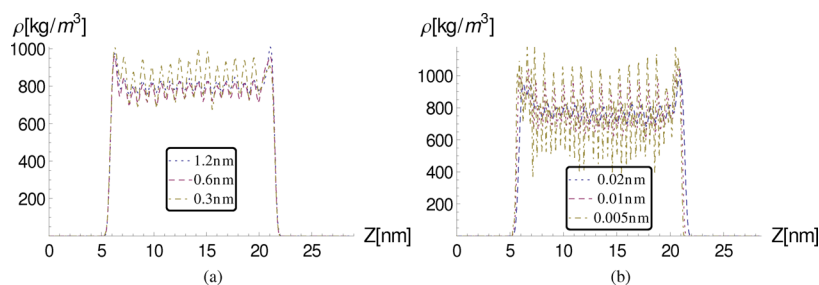
Figure 4. Influence of binwidths on density for the hydrate−oil systems: (a) tangential binwidths, bwn = 0.02 nm; (b) normal binwidths, bw = 0.6 nm. Only water molecules are shown for clarity, Gaussian filter order 20, same trajectory frame.
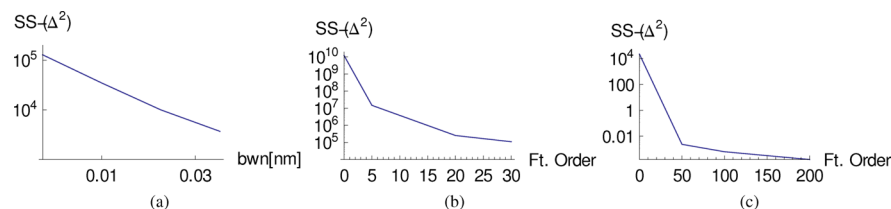
Figure 5. Smoothness (see eq 7) changes of order parameter profiles with filter order and normal binwidth: (a) hydrate−oil, density, normal binwidth; (b) hydrate−oil, density, filter order; (c) hydrate−water, F_4, filter order.
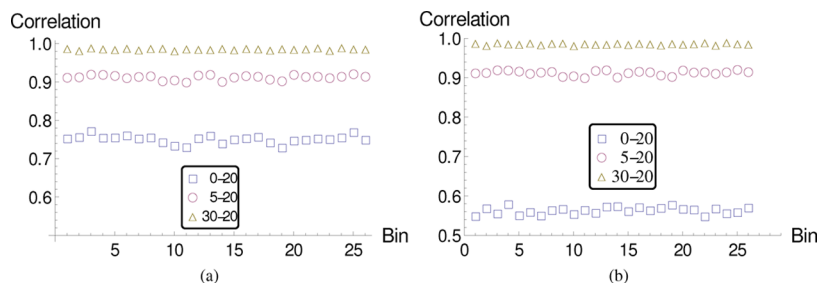
Figure 6. Spatial−spatial cross-correlation of the density parameter profiles at same time and normal-to-interface spatial location, using different filter order combinations, as a function of in-interface position: (a) hydrate−oil and (b) ice−oil.
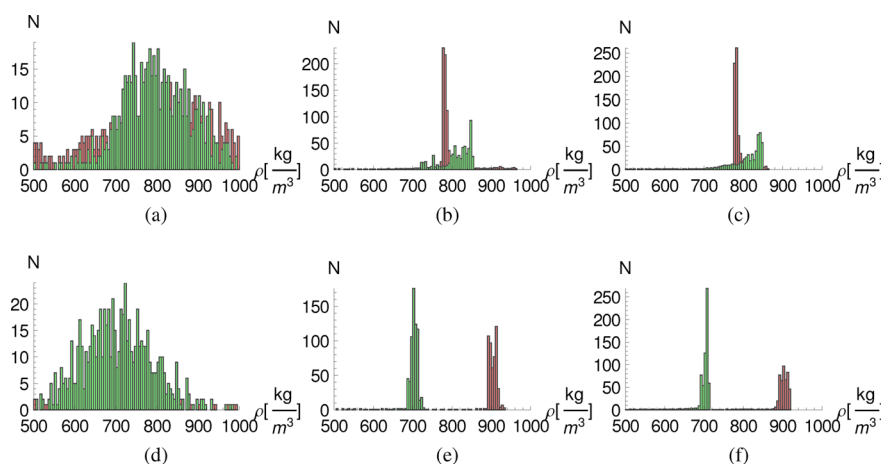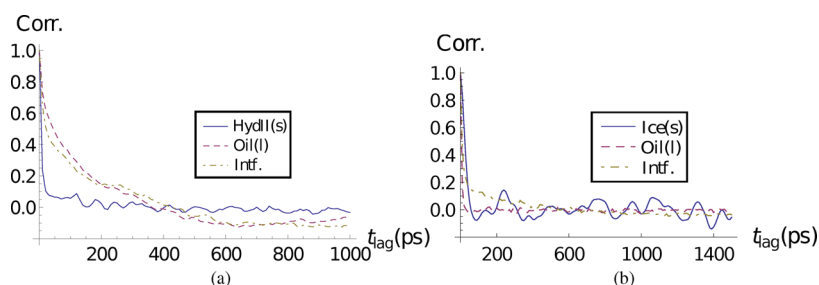

Figure 7. Density order parameter distributions in the hydrate−oil and ice−oil systems for a single trajectory frame, t = 500 ps, averaged over all interfacial strips, using different filter orders (red, waters; green, octane): (a−c) hydrate−oil with filter order 0 (no filter), 20, and 50, respectively; (d−f) ice−oil with filter order 0, 30, and 60, respectively.

fixed shape. Note also that the correlations between the profiles with higher filter orders are very strong, indicating that little is gained in smoothness and consistency from increasing the filter order much above 30 with the present system sizes.

3.1.5. Phase Distinguishability. The distributions of the density order parameters, focusing on the waters and oil separately, are illustrated by both the distributions of all trajectory frames (Figure S2) and that of an individual frame (Figure 7a). The density difference between hydrate−water, ρ_{hw} = 800 kg/m^3, and octane, $\rho_{oct} \approx$ 720 kg/m^3, is small. Because of this it may seem difficult to separate the phases fully, even with high filter orders. In fact, at first glance the oil density seems

Figure 8. Density parameter−time autocorrelation for (a) hydrate-II−oil and (b) ice-1H−oil, averaged over all 1D strips for Gaussian filter of order 50 in different phases.
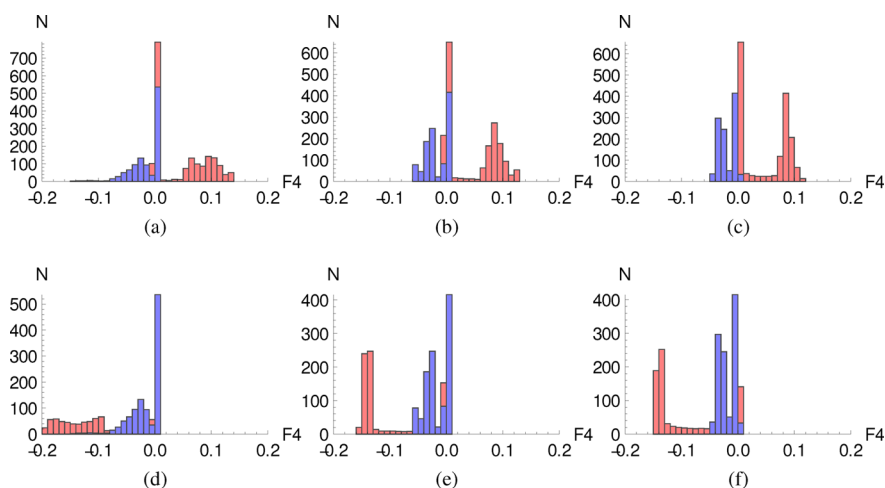
Figure 9. F_4 order parameter distributions in hydrophilic interfaces. Red columns are for hydrate−ice H_2O, blue columns for liquid H_2O; single trajectory frame, averaged over all in-interface profiles using different order Gaussian filters: (a−c) hydrate-II−water, order 10, 50, and 100, respectively; (d−f) ice-1H−water with corresponding filter orders.

slightly higher than the water density in the filtered profiles in the figures; note, however, the long tail of the distributions, particularly the water distributions. If we exploit the fact that there are volumes in the box where the water and oil components, respectively, are absent, this difficulty can be overcome by considering the interface region to be where the respective densities become zero for either oil or water. The difference in octane density between the ice and hydrate systems is probably due to some residual alignment of the octane molecules in the hydrate system as mentioned in section 2.1.1, in spite of having increased the system width to mitigate this.

The decreasing influence of filter widths above 30 for distinguishability is illustrated by computing the ratios of variances of those densities falling within certain bands around the peaks shown in Figure 7a and all the densities in the computational box, and comparing these ratios for different filter widths. The bands chosen were $\Delta\rho = 400$ and 500 kg/m^3. This is shown in the Supporting Information for time $t = 50$ ps. Widening the filter to more than order 30 reduces distinguishability between the peaks for both water and octane components.

The quality of the temporal sampling is shown by the time autocorrelation of the density parameter for three distinct Z values corresponding to the location of the different phases in the simulation box (Figure 8a). This shows that the solid phase has an appreciably smaller correlation time compared to the liquid phase. The presence of small but quite clear oscillations in the autocorrelation at higher time lags for the crystals is visible, possibly indicating the presence of a series of phonons.

3.2. The Ice-IH−Oil Interface. Since the results are broadly similar to those for hydrate−oil systems, only the most notable differences are discussed here. For ice−oil interfaces (Figure 1c) a slightly higher filter order is needed than for hydrate−oil, because the smoothness is lower for the ice−oil system (Figure S1). A Gaussian filter width of 30 was used for the ice−oil systems to obtain smoothness comparable to that obtained with a filter width of 20 for hydrate−oil. The spatial−spatial correlations of different filter orders is shown in Figure 6a, which can be compared to Figure 6b, showing that there is lower correlation between profiles in the ice−oil case. This is mainly due to stronger noise in the ice−oil system; the authors are, at present, not sure why the noise should be stronger in this system.

The influence of tangential binwidth in this system is very similar to the hydrate−oil case and will therefore not be shown further here. The normal binwidth appears to have slightly stronger effect on the ice−oil system than for hydrate−oil, as noted by careful comparison of Figure S1 with Figure 4b, where a more pronounced narrowing of the profile with decreased binwidth in combination with a much more severe decrease in smoothness at the smallest binwidths is visible for the ice−oil system, indicating that a binwidth smaller than 0.01 nm is not suitable for use with ice. Figure 7d shows that distinguishability is less of an issue with ice−oil than with hydrate−oil, because of the higher density difference. However, a mild filtering is still needed to distinguish the phases, as the raw density field oscillates in the range 0−2500 kg/m^3 at the same normal binwidth.

The temporal behavior of the ice−oil system is different from the hydrate−oil case, as can be seen by comparing Figure 8a with
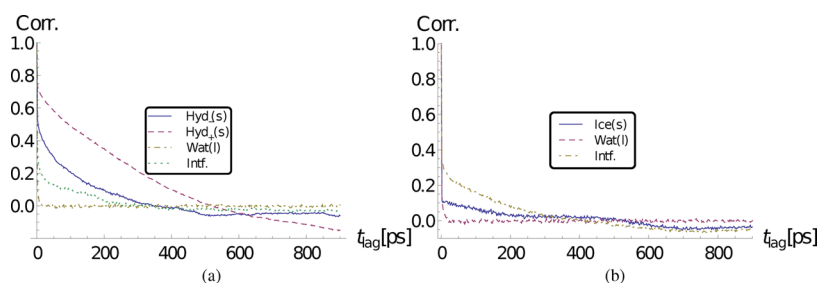
Figure 10. F_4 parameter−time autocorrelation for (a) hydrate-II−water and (b) ice-IH−water, averaged over all 1D strips for Gaussian filter of order 50 in different phases.
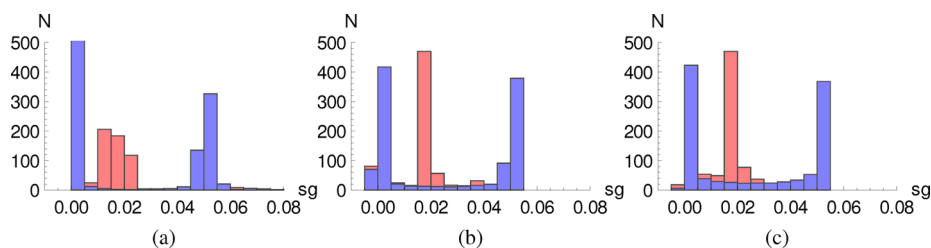
Figure 11. Tetrahedral angle order parameter distributions in the ice−water interface for a single trajectory frame averaged over all in-interface profiles using different order Gaussian filters: (a) 10, (b) 50, (c) 100. Red columns are for ice H_2O, blue columns for liquid H_2O.

Figure 8b. The more correlated ice-crystal motion is evident, which actually reverses the order of correlation times, such that the correlation time in oil is shorter than the correlation time in the ice phase.

3.3. The Hydrate-II−Water Interface. The tetrahedral order parameter is not useful for the hydrate−water interface (Figure 1b) since both phases are strongly tetrahedrally coordinated. Slight differences in order parameters can be observed between the phases using both the tetrahedral distance and angle parameters, but neither shows enough distinguishability to clearly separate the phases. The F_4 parameter, in contrast, shows clearly different values for hydrate-II and bulk water. This is mainly due to the planar H-bonded rings that are present in the hydrate phase but not in cold water.

The influence of filter width on smoothness is shown in Figure 5c for the same system with bw = 0.6 nm, bwn = 0.02 nm for a single frame. From Figure S3, it is clear that the filter width applied should be minimized to avoid moving the interface position and reducing the resolution for interface movement. Reducing the filter width too much will compromise the demarcation scheme, however.

We now turn to the question of distinguishability of the phases by means of the order parameter and filtering approach. The phases are colored in accordance with the original phase index in Figure 9. There is overlap from the hydrate and ice phases into liquid water parameter values, and this is the primary reason for the need of a filtering step. At a filter width of about 100, the hydrate peak in the liquid water range can be seen to have decreased appreciably. The overlap is in part due to melting of molecules on the hydrate and ice surfaces, respectively. If we ignore the coloring, we note that the peaks in the distribution are rather distinct, such that the F_4 order parameter can indeed be used to distinguish the different water phases.

The dynamics of the order parameters are pictured in the time autocorrelation maps for the entire system and for the different phases in Figure 10a. The correlation time for the water phase is very short; furthermore, as expected, there are relatively strong

correlations in the motions of the hydrate structure, yielding longer correlation times here.

3.4. Ice−Water System. The ice−water interface (Figure 1d) can be detected and distinguished by both the tetrahedral and the F_4 order parameters, as displayed in Figures 9 and 11. Both order parameters separate the phases well, with the added complication that the tetrahedral parameter has an additional separate, equal-magnitude peak for the water phase. The F_4 parameter, too, shows overlap between an additional smaller peak from the ice-IH phase within the water range, but this peak is less prominent. The only dominating peak at low order is the shared peak at $F_4 = 0$, whereas with increasing filter order, a secondary ice peak at $F_4 = 0.15$ is visible at filter orders ≥ 50. The peak at $F_4 = 0$ is suppressed for the ice phase at higher filter orders.

A similar trend can be seen in histograms averaged over the entire trajectory (Figure S4), where the benefits of modest filtering in suppressing the shared peak around $F_4 = 0$ are more clearly discerned. A low-pass filter has little effect on the relative magnitude of the peaks but seems to separate the overlap, particularly at high filter order. It thus seems that the F_4 order parameter is the best for distinguishing ice and water, all else being equal.

The time autocorrelation behaves differently for the ice−water system, as shown in Figure 10b. There is hardly any correlation observable except in the interface region. The correlation time in the ice phase is significantly shorter than in the hydrate phase, whereas in the other phases, including the interface, the correlation times are similar.

4. DISCUSSION

4.1. Order Parameters. Density fields can be used to distinguish phases in a hydrate (ice)−oil interface provided a suitable low-pass filter is applied combined with an appropriate meshing scheme (Figure 2c,d). Similarly the dihedral angle parameter, F_4, can be applied to dynamically probe the hydrate (ice)−water interfaces (Figure 1b,d) whereas the tetrahedrality parameter is only feasible for use with ice−water (Figure 1d), due

Table 1. Effective Time Steps t_{step} and Autocorrelation Times t_{corr} of Order Parameters in Each Phase in the Simulation Box (Mass Density in the Water−Oil, Respectively F_4 in the Water−Water-Type Systems)

system	phase	t_{step} (ps)	t_{corr}[a] (ps)
hydrate−oil	hydrate	2	5(1)
	oil	2	60(2)
	interface	2	53(3)
ice−oil	ice	2	22.7(7)
	oil	2	1.70(4)
	interface	2	4.3(2)
hydrate−water	hydrate	2	43(2)
	water	2	0.97(3)
	interface	2	8.1(8)
ice−water	ice	2	152(9)
	water	2	1.08(2)
	interface	2	127(5)

[a]Values within parentheses give error in the last digit.

to the strong similarity in tetrahedrality between the hydrate−water cages and icy-cold water.

As the F_4 parameter matches the tetrahedral parameter in its ability to distinguish ice and water, it has the best distinguishing ability overall in solid−liquid water systems of ice-1H and hydrate. In hydrate−water or ice−water systems the possibility that water molecules go from one phase to the other (by freezing or melting) means that we can not distinguish components based on the phase the molecules were in at the start of the simulation. However, this is not a drawback of either of the order parameters. In applications one would probably like to be able to distinguish the phases without prior knowledge, and the distributions of order parameters in Figures 7a,d (density), 9 (F_4), and 11 (S_g) indicate that this is quite possible.

The order parameters studied here are found to be relatively insensitive toward altering the in-interface binwidth, provided this is somewhat larger than the molecular size of the species studied. The density field is sensitive to the normal binwidth and filter width, in terms of both consistency of location and interface width.

The F_4 parameter gives noisier raw profiles, and thus requires higher filter orders and/or larger normal binwidths than the density parameter. In systems containing water this is due to the significant fluctuations encountered.

Scaling the Gaussian filter order and normal binwidth inversely yields invariant profiles over large parameter ranges in the density

field, whereas the F_4 parameter shows less tolerance to the same transformation, highlighting that methods for distinguishing different phases are highly system dependent.

Both the smoothness and the distinguishing ability of the order parameters increase with filter width, however with decreasing returns with increasing width.

Some understanding of the dynamical behavior of the order parameters is obtained from the time autocorrelation maps given in the Supporting Information. In the systems containing a hydrophobic phase, the interface region is appreciably larger for hydrate than for ice. In addition, the hydrate−oil interface shows distinctly more correlated motions than the ice−oil interface. This larger degree of interaction can probably be partly explained by the dynamical exchange of propanes between the hydrate and the oil phase.

Representative autocorrelation times of the order parameter fields in the different systems are shown in Table 1, extracted from data shown in Figures 8 and 10b using no time averaging (t_{step} = 2 ps) and with time-block averaging of 5 blocks (t_{step} = 10 ps).

There appear to be much longer lasting correlations in the ice−water interface than in the hydrate−water interface. The ice phase itself shows much larger dynamical correlations in water than in oil.

4.2. Hydrophilic/Hydrophobic Spectra. The fluctuation spectra of the ice−oil system are given in Figure 12b and those for hydrate−oil in Figure 12a. The figures show fluctuations in both interfaces in the B-A-B system topology. The numerical details of the analysis are summarized in Figure 2. As is clearly seen, only the last hydrate−oil interface shows results that are reasonably close to their expected real values.

The CWF theory dictates that at low k the fluctuation magnitude $|C[k]|^2$ varies with $1/k^2$, i.e., a slope of −2 in the log−log plots in Figure 12. Only the hydrate−oil interfaces give rise to such a fit, though a single interface of the ice−oil-1 simulation is within 3 standard deviations of it according to Table 2. In the ice−water and hydrate−water systems, there is too much noise to identify a linear relationship with the present methodology.

It is believed that the main barrier to achieving a better outcome is the coarse meshing of the normal-to-interface motions. Such enforced resolution limits leads to under-estimation of the magnitude of interfacial fluctuations if, as we suspect, the magnitudes of the higher frequency fluctuations are comparable to or smaller than the mesh size in the normal direction. This again leads to overestimation of the interfacial stiffness (and interfacial free energy) when the stiffness of the system rises above a certain threshold.
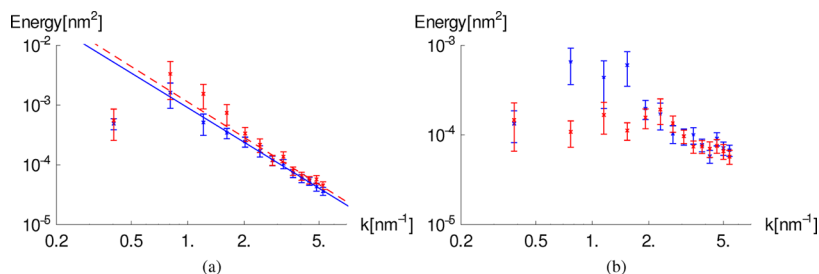
Figure 12. Interface fluctuation power spectra of hydrate (a) and ice (b) in oil. Lines show best fit to straight line for the hydrate−oil case: blue, interface 1; red, interface 2 (cf. Figure 2).

Table 2. Summary of Interfacial Fluctuations of the Systems in Oil

system	trajectory t (ps)	trajectory t_{step} (ps)	L (nm)	b (nm)	interface t_{corr} (ps)	slope (−)	adjusted R^2 (−)	interface stiffness (mN/m)
ice−oil-1	500	0.2	16.3586(2)	2.3623(1)	60(40)	−1.5(2)	0.85	170(30)
						−0.9(2)	0.64	400(100)
ice−oil-2	3000	10	16.358(4)	2.3626(7)	160(70)	−1.2(2)	0.70	230(50)
						−0.8(2)	0.67	300(200)
hydrate−oil	2000	10	15.568(2)	3.5(1)	210(90)	−1.93(4)	0.99	76(4)
						−1.9(2)	0.91	65(15)

5. CONCLUSIONS

In summary, we find that the density fields in combination with a suitable meshing scheme and low-pass filter can be used to distinguish phases in a hydrate (ice)−oil interface. The dihedral angle parameter, F_4, can be used probe the hydrate (ice)−water interfaces also dynamically. The tetrahedrality parameter is also usable, but only with ice−water systems, due to the strong similarity in tetrahedrality between the hydrate−water cages and icy-cold water.

The data on autocorrelation show that there are longer lasting correlations in the ice−water interface than in the hydrate−water interface. The ice phase itself shows larger dynamical correlations in water than in oil.

■ ASSOCIATED CONTENT

Ⓢ Supporting Information

Additional figures showing the effect of normal binwidth on the density order parameter in the ice−oil system, the effect of filter order on surface distinguishability based on the density order parameter, distributions of density order parameter for various filter orders, effect of filter order on the spatial distribution of the F_4 order parameter, distributions of the F_4 order parameter in hydrophilic interfaces for various filter orders, distributions of the tetrahedrality order parameter for various filter orders, and time autocorrelation maps as a function of normal to interface direction Z. This material is available free of charge via the Internet at http://pubs.acs.org.

■ AUTHOR INFORMATION

Corresponding Author

*E-mail: bjorn.sathre@ift.uib.no.

Notes

The authors declare no competing financial interest.

■ REFERENCES

(1) Sum, A. K.; Koh, C. A.; Sloan, E. D. Developing a comprehensive understanding and model of hydrate in multiphase flow: from laboratory measurements to field applications. *Energy Fuels* **2012**, *26*, 4046−4052.

(2) Wenqing, L.; Jing, G.; Xiaofang, L.; Jiankui, Z.; Yaorong, F.; Da, Y. A study of hydrate plug formation in a subsea natural gas pipeline using a novel high-pressure flow loop. *Pet. Sci.* **2013**, *10*, 97−105.

(3) Zerpa, L. E.; Salager, J.-L.; Koh, C. A.; Sloan, E. D.; Sum, A. K. Surface Chemistry and Gas Hydrates in Flow Assurance. *Ind. Eng. Chem. Res.* **2011**, *50*, 188−197.

(4) Creek, J. L. Efficient Hydrate Plug Prevention. *Energy Fuels* **2012**, *26*, 4112−4116.

(5) Kashchiev, D.; Firoozabadi, A. Induction time in crystallization of gas hydrates. *J. Cryst. Growth* **2003**, *250*, 499−515.

(6) Pirzadeh, P.; Kusalik, P. G. Molecular Insights into Clathrate Hydrate Nucleation at an Ice-Solution Interface. *J. Am. Chem. Soc.* **2013**, *135*, 7278−7287.

(7) Leba, H.; Cameirao, A.; Herri, J.; Darbouret, M.; Peytavy, J.; Glenat, P. Chord length distributions measurements during crystal-

lization and agglomeration of gas hydrate in a water-in-oil emulsion: Simulation and experimentation. *Chem. Eng. Sci.* **2010**, *65*, 1185−1200.

(8) Smith, J. D.; Meuler, A. J.; Bralower, H. L.; Venkatesan, R.; Subramanian, S.; Cohen, R. E.; McKinley, G. H.; Varanasi, K. K. Hydrate-phobic surfaces: fundamental studies in clathrate hydrate adhesion reduction. *Phys. Chem. Chem. Phys.* **2012**, *14*, 6013−6020.

(9) Du, J.; Wang, Y.; Lang, X.; Fan, S. Effects of polyvinyl alcohol on the adhesion force of tetrahydrofuran hydrate particles. *Energy Fuels* **2011**, *25*, 3204−3211.

(10) Bonnefoy, O.; Gruy, F.; Herri, J. M. Van der Waals interactions in systems involving gas hydrates. *Fluid Phase Equilib.* **2005**, *231*, 176−187.

(11) Bergflodt, L.; Gjertsen, L. H.; Sjoblom, J.; Kallevik, H.; Oye, G. Chemical influence on the formation, agglomeration, and natural transportability of gas hydrates. A multivariate component analysis. *J. Dispersion Sci. Technol.* **2004**, *25*, 355−365.

(12) Aman, Z. M.; Dieker, L. E.; Aspenes, G.; Sum, A. K.; Sloan, E. D.; Koh, C. A. Influence of model oil with surfactants and amphiphilic polymers on cyclopentane hydrate adhesion forces. *Energy Fuels* **2010**, *24*, 5441−5445.

(13) Kashchiev, D.; Firoozabadi, A. Driving force for crystallization of gas hydrates. *J. Cryst. Growth* **2002**, *241*, 220−230.

(14) Sefidroodi, H.; Chua, P. C.; Kelland, M. A. THF hydrate crystal growth inhibition with small anionic organic compounds and their synergistic properties with the kinetic hydrate inhibitor poly(N-vinylcaprolactam). *Chem. Eng. Sci.* **2011**, *66*, 2050−2056.

(15) Sun, M.; Wang, Y.; Firoozabadi, A. Effectiveness of alcohol cosurfactants in hydrate antiagglomeration. *Energy Fuels* **2012**, *26*, 5626−5632.

(16) Norland, A. K.; Kelland, M. A. Crystal growth inhibition of tetrahydrofuran hydrate with bis- and polyquaternary ammonium salts. *Chem. Eng. Sci.* **2012**, *69*, 483−491.

(17) Sathre, B. S.; van der Spoel, D.; Hoffmann, A. C. Free energy of separation of structure II clathrate hydrate in water and a light oil. *J. Phys. Chem. B* **2012**, *116*, 5933−5940.

(18) Gaillard, C. L. R. Investigation of methane hydrate formation in a recirculating flow loop: Modeling of the kinetics and tests of efficiency of chemical additives on hydrate inhibition. *Rev. Inst. Fr. Pet.* **1999**, *54*, 365−374.

(19) Ribeiro, C.; Lage, P. L. C. Modelling of hydrate formation kinetics: State-of-the-art and future directions. *Chem. Eng. Sci.* **2008**, *63*, 2007−2034.

(20) Makogon, Y. F. Experiments illustrate hydrate morphology, kinetics. *Oil Gas J.* **2001**, *99*, 45−50.

(21) Kvamme, B.; Graue, A.; Aspenes, E.; Kuznetsova, T.; Granasy, L.; Toth, G.; Pusztai, T.; Tegze, G. Kinetics of solid hydrate formation by carbon dioxide: Phase field theory of hydrate nucleation and magnetic resonance imaging. *Phys. Chem. Chem. Phys.* **2004**, *6*, 2327−2334.

(22) English, N. J.; MacElroy, J. M. D. Theoretical studies of the kinetics of methane hydrate crystallization in external electromagnetic fields. *J. Chem. Phys.* **2004**, *120*, 10247−10256.

(23) Sinquin, A.; Palermo, I.; Peysson, Y. Rheological and flow properties of gas hydrate suspensions. *Oil Gas Sci. Technol.* **2004**, *59*, 41−57.

(24) Delahaye, A.; Fournaison, L.; Jerbi, S.; Mayoufi, N. Rheological properties of CO2 hydrate slurry flow in the presence of additives. *Ind. Eng. Chem. Res.* **2011**, *50*, 8344−8353.

(25) Wang, W.; Fan, S.; Liang, D.; Li, Y. A model for estimating flow assurance of hydrate slurry in pipelines. *J. Nat. Gas Chem.* **2010**, *19*, 380−384.

(26) Aman, Z. M.; Brown, E. P.; Sloan, E. D.; Sum, A. K.; Koh, C. A. Interfacial mechanisms governing cyclopentane clathrate hydrate adhesion/cohesion. *Phys. Chem. Chem. Phys.* **2011**, *13*, 19796−19806.

(27) Aman, Z. M.; Olcott, K.; Pfeiffer, K.; Sloan, E. D.; Sum, A. K.; Koh, C. A. Surfactant adsorption and interfacial tension investigations on cyclopentane hydrate. *Langmuir* **2013**, *29*, 2676−2682.

(28) Walsh, M. R.; Koh, C. A.; Sloan, E. D.; Sum, A. K.; Wu, D. T. Microsecond simulations of spontaneous methane hydrate nucleation and growth. *Science* **2009**, *326*, 1095−1098.

(29) Schrader, M.; Virnau, P.; Winter, D.; Zykova-Timan, T.; Binder, K. Methods to extract interfacial free energies of flat and curved interfaces from computer simulations. *Eur. Phys. J.: Spec. Top.* **2009**, *177*, 103−127.

(30) Steinhardt, P. J.; Nelson, D. R.; Ronchetti, M. Bond-orientational order in liquids and glasses. *Phys. Rev. B* **1983**, *28*, 784−805.

(31) Radhakrishnan, R.; Trout, B. L. A new approach for studying nucleation phenomena using molecular simulations: Application to CO2 hydrate clathrates. *J. Chem. Phys.* **2002**, *117*, 1786−1796.

(32) Matsumoto, M.; Baba, A.; Ohmine, I. Topological building blocks of hydrogen bond network in water. *J. Chem. Phys.* **2007**, *127*, No. 134504.

(33) Jacobson, L. C.; Matsumoto, M.; Molinero, V. Order parameters for the multistep crystallization of clathrate hydrates. *J. Chem. Phys.* **2011**, *135*, No. 074501.

(34) Hoyt, J. J.; Asta, M.; Karma, A. Method for computing the anisotropy of the solid-liquid interfacial free energy. *Phys. Rev. Lett.* **2001**, *86*, 5530−5533.

(35) Angioletti-Uberti, S.; Ceriotti, M.; Lee, P. D.; Finnis, M. W. Solid-liquid interface free energy through metadynamics simulations. *Phys. Rev. B* **2010**, *81*, No. 125416.

(36) Davidchack, R. L.; Morris, J. R.; Laird, B. B. The anisotropic hard-sphere crystal-melt interfacial free energy from fluctuations. *J. Chem. Phys.* **2006**, *125*, No. 094710.

(37) Becker, C. A.; Olmsted, D. L.; Asta, M.; Hoyt, J. J.; Foiles, S. M. Atomistic simulations of crystal-melt interfaces in a model binary alloy: Interfacial free energies, adsorption coefficients, and excess entropy. *Phys. Rev. B: Condens. Matter Mater. Phys.* **2009**, *79*, No. 054109.

(38) Rozas, R. E.; Horbach, J. Capillary wave analysis of rough solid-liquid interfaces in nickel. *Europhys. Lett.* **2011**, *93*, No. 26006.

(39) Feng, X.; Laird, B. B. Calculation of the crystal-melt interfacial free energy of succinonitrile from molecular simulation. *J. Chem. Phys.* **2006**, *124*, No. 44707.

(40) Tarazona, P.; Checa, R.; Chacon, E. Critical Analysis of the Density Functional Theory Prediction of Enhanced Capillary Waves. *Phys. Rev. Lett.* **2007**, *99*, No. 196101.

(41) Rowlinson, J. S.; Widom, B. *Molecular Theory of Capillarity*; International Series of Monographs on Chemistry; Clarendon Press: Oxford, 1984.

(42) Gelfand, M. P.; Fisher, M. E. Finite Size-effects in fluid interfaces. *Physica A* **1990**, *166*, 1−74.

(43) Hoyt, J. J.; Asta, M.; Karma, A. Atomistic and continuum modeling of dendritic solidification. *Mater. Sci. Eng.: R: Reports* **2003**, *41*, 121−163.

(44) Mecke, K. R.; Dietrich, S. Effective Hamiltonian for liquid-vapor interfaces. *Phys. Rev. E* **1999**, *59*, 6766−6784.

(45) Vink, R. L. C.; Horbach, J.; Binder, K. Capillary waves in a colloid-polymer interface. *J. Chem. Phys.* **2005**, *122*, No. 134905.

(46) Hayward, J. A.; Reimers, J. R. Unit cells for the simulation of hexagonal ice. *J. Chem. Phys.* **1997**, *106*, 1518−1529.

(47) Abascal, J. L. F.; Sanz, E.; Fernandez, R. G.; Vega, C. A potential model for the study of ices and amorphous water: TIP4P/Ice. *J. Chem. Phys.* **2005**, *122*, No. 234511.

(48) Jorgensen, W. L.; Madura, J. D.; Swenson, C. J. Optimized intermolecular potential functions for liquid hydrocarbons. *J. Am. Chem. Soc.* **1984**, *106*, 6638−6646.

(49) Miyamoto, S.; Kollmann, P. SETTLE—an analytical version of the shake and rattle algorithm for rigid water models. *J. Comput. Chem.* **1992**, *13*, 952−962.

(50) Essmann, U. A smooth particle mesh Ewald method. *J. Chem. Phys.* **1995**, *103*, 8577−8593.

(51) Berendsen, H. J. C.; Postma, J. P. M.; van Gunsteren, W. F.; Dinola, A.; Haak, J. R. Molecular-Dynamics with coupling to an external bath. *J. Chem. Phys.* **1984**, *81*, 3684−3690.

(52) Bussi, G.; Donadio, D.; Parrinello, M. Canonical sampling through velocity rescaling. *J. Chem. Phys.* **2007**, *126*, No. 014101.

(53) Hess, B.; Kutzner, C.; van der Spoel, D.; Lindahl, E. GROMACS 4.0: Algorithms for highly efficient, load-balanced, and scalable molecular simulation. *J. Chem. Theory Comput.* **2008**, *4*, 435−447.

(54) Chau, P. L.; Hardwick, A. J. A new order parameter for tetrahedral configurations. *Mol. Phys.* **1998**, *93*, 511−518.

(55) Rodger, P. M.; Forester, T. R.; Smith, W. Simulations of the methane hydrate/methane gas interface near hydrate forming conditions conditions. *Fluid Phase Equilib.* **1996**, *116*, 326−332.